Operation of a load current multiplier on a nanosecond mega-ampere pulse forming line generator

A. S. Chuvatin,[1] V. L. Kantsyrev,[2] L. I. Rudakov,[3] M. E. Cuneo,[4] A. L. Astanovitskiy,[2] R. Presura,[2] A. S. Safronova,[2] W. Cline,[2] K. M. Williamson,[2] I. Shrestha,[2] G. C. Osborne,[2] B. LeGalloudec,[2] V. Nalajala,[2] T. D. Pointon,[4] and K. A. Mikkelson[4]

[1]*Laboratoire de Physique des Plasmas, Ecole Polytechnique, Palaiseau 91128, France*
[2]*University of Nevada Reno, Reno, Nevada 89557, USA*
[3]*Icarus Research, Inc., P.O. Box 30780, Bethesda, Maryland 20824, USA*
[4]*Sandia National Laboratories, Albuquerque, New Mexico 87185, USA*
(Received 8 November 2008; published 25 January 2010)

We investigate the operation of a load current multiplier (LCM) on a pulse-forming-line nanosecond pulse-power generator. Potential benefits of using the LCM technique on such generators are studied analytically for a simplified case. A concrete LCM design on the Zebra accelerator (1.9 Ohm, ~1 MA, 100 ns) is described. This design is demonstrated experimentally with high-voltage power pulses having a rise time of dozens of nanoseconds. Higher currents and magnetic energies were observed in constant-inductance solid-state loads when a better generator-to-load energy coupling was achieved. The load current on Zebra was increased from the nominal 0.8–0.9 MA up to about 1.6 MA. This result was obtained without modifying the generator energetics or architecture and it is in good agreement with the presented numerical simulations. Validation of the LCM technique at a nanosecond time scale is of importance for the high-energy-density physics research.

DOI: 10.1103/PhysRevSTAB.13.010401 PACS numbers: 84.70.+p, 84.60.Ve

Megagauss-range magnetic fields are widely applied in high-energy-density physics, plasma physics, solid-state physics, such as studies of material properties under high dynamic pressures, etc. [1]. Some applications including fast heating of highly radiating materials, inertial plasma confinement, or generation of strong shocks require also the shortest possible times of the magnetic energy release [2]. The most developed approach allowing high current pulses (mega-amperes) with short ($\sim 10^{-7}$ s) rise times is the pulsed-power technique based on pulse forming lines (PFL) [3]. In this technique, high magnetic fields can be obtained at small millimeter-scale diameters, usually in a solid-state or plasma load.

However, this approach requires more than tenfold concentration of the electromagnetic power in space from the large-size (dozens of centimeters) dielectric-insulated PFL output to a small, centimeter-scale vacuum volume representing the high magnetic energy density load. For a given value of the PFL voltage V_{oc}, the minimum physical volume necessary for electric connections to the load is constrained by high-voltage dielectric and vacuum insulation strengths. The higher the voltage V_{oc}, the larger the connection volume and the higher its self-inductance L_0. In turn, the PFL impedance ρ limits the maximum accessible load current amplitude I_0 to V_{oc}/ρ. The rise time $\tau \propto L_0/\rho$ of $I_0(t)$ is thus limited from below by the minimum L_0 volume which still ensures lossless energy delivery to the load [3]. A practical compromise between higher I_0 and smaller τ attainable at the present technology level of mega-ampere PFL's with $\tau \sim 100$ ns results in $L_0 \geq$ 10–20 nH.

At the same time, high magnetic energy densities are achievable in small load volumes which can have inductance L_d of only units of nanohenries, so that $L_d \ll L_0$. At a given I_0 constrained by ρ, by V_{oc} and thus by L_0, see above, the driver-to-load energy transfer efficiency defined by the ratio $\eta = L_d/(L_0 + L_d)$ can be also small. New generation pulse-power drivers with petawatt-range electromagnetic power would require an almost threefold increase of V_{oc} and L_0 [4], while the load volume and inductance L_d, or its variation ΔL_d remain unchanged for useful applications such as inertial confinement fusion [3]. This would lead to a further decrease of the efficiency η. It seems that a dramatic increase of I_0 can be accessible only through the increase of the generator output voltage [3,4] that would require a larger and more expensive pulse-power system with larger L_0 and lower η.

The purpose of this paper is to demonstrate this is not always true and to show how the load magnetic energy can be enhanced without changing the generator architecture by decreasing ρ and/or increasing the generator stored energy to allow V_{oc} to be increased. We demonstrate a different approach to increasing the load current, the load current multiplier (LCM) [5]. This recently suggested method operates as an impedance transformer and increases the load magnetic energy. LCM's were previously tested with low-voltage, microsecond capacitor discharges [6] but have never been applied on PFL high-voltage,

nanosecond-pulse generators. We now show an increase of the current by a factor of 1.88 ± 0.38, for 100 ns pulses with this technique on a nanosecond PFL generator Zebra [7–9] in the University of Nevada, Reno.

A PFL-based generator can be characterized by its wave impedance ρ and by the open-circuit voltage V_{oc} at the dielectric-vacuum insulator [10]. The insulator and vacuum lines delivering the power to a load have some irreducible inductance L_0 which is limited from above by the minimum possible interelectrode gaps still allowing one to avoid insulator breakdown and electron current losses and plasma shorting of the vacuum gaps [3].

The Zebra generator [9] has an architecture typical for PFL-based pulse-power facilities and it is routinely used for production of strong magnetic fields [11] and in experimental z-pinch physics research [12]. Figure 1 shows the output section in standard generator operation with solid-state or plasma loads. We further consider only inductive loads having constant inductance L_d. Configurations of Fig. 1 then are described by the following equation [10]:

$$(L_0 + L_{dc} + L_d)\frac{dI_0}{dt} + \rho I_0 = V_{oc}, \tag{1}$$

where I_0 is the output current and the inductances L_0, L_{dc}, and L_d are explained in the notation to Fig. 1.

Study a simplified case when the open-circuit voltage is constant, i.e., it instantaneously rises to the value V_{oc} at $t = 0$ and then remains unchanged. In other words, the voltage rise time $t_{0\,V} = 0$ in this approximation. Solution of Eq. (1) is

$$I_0 = \frac{V_{oc}}{\rho}\left[1 - \exp\left(-\frac{\rho}{L_{tot}}t\right)\right], \tag{2}$$

where $L_{tot} \equiv L_0 + L_{dc} + L_d$. For $t \to \infty$, the generator and load current I_0 tends to the short-circuit value V_{oc}/ρ. Let us define the characteristic load current rise time as $t_0 \equiv 2L_{tot}/\rho$ and let us introduce the characteristic load current amplitude $I_0{}^{max}$ as the current value at $t = t_0$, when $I_0{}^{max} \equiv I_0(t_0) \approx 0.86V_{oc}/\rho$:

$$I_0{}^{max} \equiv I_0(t_0) = \frac{V_{oc}}{\rho}(1 - e^{-2}). \tag{3}$$

Compare this simple estimate to a typical experimental result in standard Zebra configuration of Fig. 1. Standard Zebra parameters are $\rho = 1.9$ Ohm [7] for the generator impedance and $L_0 \approx 26$ nH for the generator inductance corresponding to the volumes (2) and (3) in Fig. 1. L_{dc} and L_d are the inductances of the diagnostic chamber (4) and load (5), respectively, and they change depending on the experiment. Figure 2 shows typical Zebra load current pulse measured in a calibration shot with $L_{dc} + L_d \approx 40$ nH ($L_{tot} \approx 66$ nH), as well as the generator open-circuit voltage $V_{oc}(t)$. The waveform of V_{oc} was derived in a separate series of experiments (not discussed here) from the voltage measurements across the insulator stack, Fig. 1, together with dI_0/dt measurements. As the experimental $V_{oc}(t)$ had shot-to-shot variation in shape and in maximum amplitude, Fig. 2 presents the averaged value over eight consecutive shots with the maximum of $V_{oc} = 1.98$ MV having a shot-to-shot variation of $\pm 13\%$. The experimental voltage rise time is $t_{0\,V} \sim 100$ ns in Fig. 2.

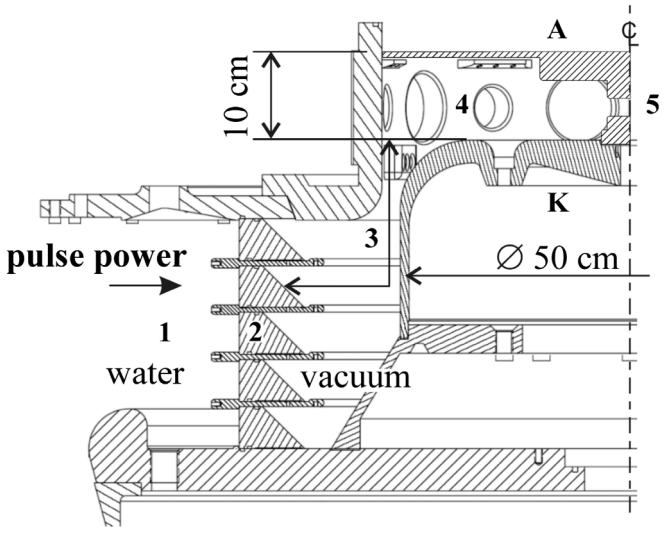

FIG. 1. Output section of the nanosecond pulse-power generator Zebra comprising (1) pulse forming line, (2) water-vacuum insulator stack, (3) vacuum pulse transmission line. Total inductance of the parts (2) and (3) is considered as the unchangeable generator inductance L_0. Diagnostic chamber (4) and the load (5) have the inductances L_{dc} and L_d, respectively. A—anode, K—cathode.

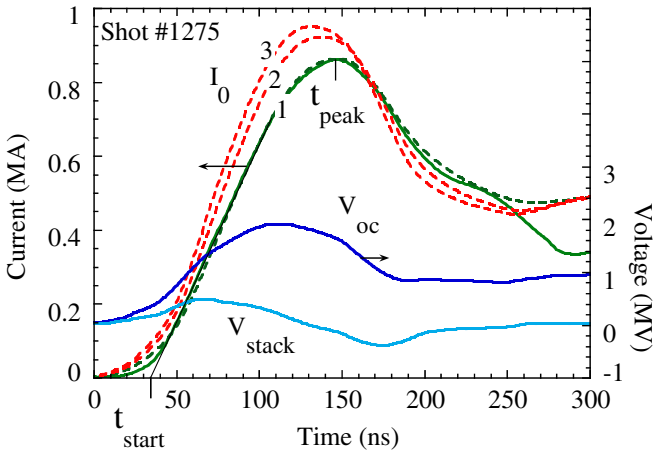

FIG. 2. (Color) Nominal short-pulse mode operation of the generator. (1) Experimental generator and load current I_0 for the shot with $L_{dc} + L_d \approx 40$ nH, solid line. Experimental averaged voltage across the stack, V_{stack}, and the unfolded open-circuit voltage V_{oc} (cannot be trusted for $t > 200$–250 ns). (1) Numerical solution $I_0(t)$ of Eq. (1) for this shot using experimental $V_{oc}(t)$, dashed line. Also shown for comparison numerical simulations with (2) $L_{dc} + L_d = 20$ nH and (3) $L_{dc} + L_d = 10$ nH.

In this calibration shot, $I_0^{\max} = 0.86$ MA and the experimental current rise time defined here and below is $t_d^{\exp} = t_{\text{peak}} - t_{\text{start}}$ (t_{peak} corresponds to the maximum I_0 and t_{start} is found from extrapolation of the linear pulse rise portion), so that experimentally $t_d^{\exp} = 114$ ns. Substitution of the maximum experimental V_{oc} value in Eq. (3) yields $I_0^{\max} \approx 0.9$ MA, which is close to the experimentally measured 0.86 MA.

At the same time, the time constant t_0 defined above, $t_0 \approx 69$ ns appears to be substantially smaller than $t_d^{\exp}$. This is because Eq. (2) was obtained, and t_0 was defined for an ideal steplike voltage waveform with $t_{0\,\text{V}} = 0$, when the current rise time is constrained only by the output inductance L_{tot} and generator impedance ρ in Eq. (1). One could conventionally discriminate here two regimes of PFL generator operation onto an inductive load: (1) the ''load-limited'' regime with $t_0 \gg t_{0\,\text{V}}$, when the load current rise time is mainly defined by L_{tot}, Eq. (2) and (2) the ''generator-limited'' regime with $t_{0\,\text{V}} \gg t_0$ and with $t_d^{\exp} \sim t_{0\,\text{V}}$. The latter case is closer to Zebra operation in its standard configuration of Fig. 1 with $L_{\text{tot}} \approx 66$ nH and $t_0 \approx 69$ ns, when $t_{0\,\text{V}} \sim 100$ ns and $t_d^{\exp} = 114$ ns $\approx t_{0\,\text{V}}$.

However, the output section of Fig. 1 will be modified following recommendations of Ref. [5] and the effective output inductance L_{tot} seen by the generator will be increased when using the load current multiplier technique, see Eq. (6) in Ref. [5] and Eq. (8) below. The simplified analysis for an ideal generator is important in this case because it shows new constraints imposed by LCM. When the output inductance increases, t_0 increases accordingly and the generator current at a given time thus should decrease.

Before we proceed with revisions of the Zebra output geometry, let us see what the maximum current the generator could provide in the standard setup of Fig. 1. Experimental dependence $V_{\text{oc}}(t)$ allows numerical solution of Eq. (2) for the calibration shot with $L_{\text{dc}} + L_d \approx 40$ nH. This numerical solution is shown in Fig. 2 (1) and it corresponds well to the experimental current waveform. Now, rearrangement of the diagnostic chamber and load electrodes (4) and (5) in Fig. 1 in order to decrease the corresponding inductance $L_{\text{dc}} + L_d$ would help somewhat in increasing the current amplitude. However, as numerical results (2) and (3) show in Fig. 2, the generator performance is not considerably improved as the peak current rises only by 10% and in any case cannot exceed the theoretical limit of $V_{\text{oc}}/\rho \sim 1$ MA.

Suppose now a modification of the Zebra output section, Fig. 1, applying the LCM technique. The load L_d is a small volume with high magnetic energy density. As described elsewhere [5], an LCM is capable to redistribute the energy between the coupling inductance L_0 and load inductance L_d operating as a transformer, or impedance adapter, and increasing the fraction of the total energy available in the system that is coupled to the load at peak current.

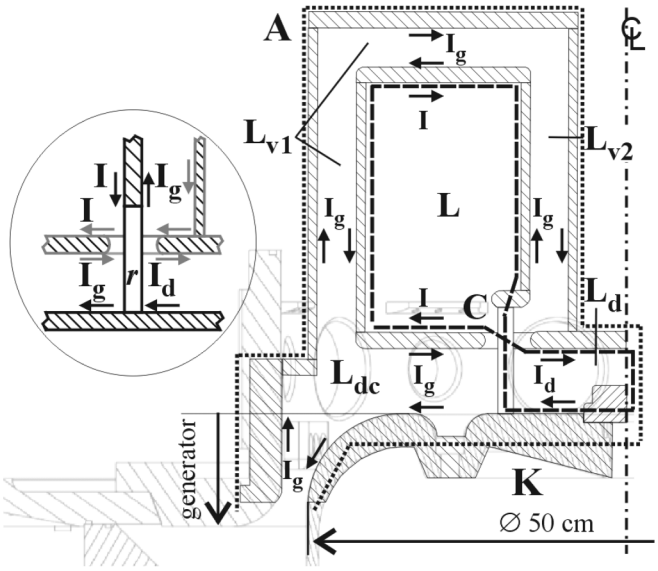

FIG. 3. A sketch of possible LCM implementation on Zebra in cylindrical geometry, cf. Fig. 1. *A*—anode, *K*—cathode. L_{dc} is the diagnostic chamber inductance between the chamber wall and the LCM convolute posts, L_v is the total bypass inductance of two coaxial and one disk lines, L_d is the load inductance, and L is inductance of the large LCM cavity. The arrows show directions of the currents in the system at the surfaces of electrodes. The current I_g powered by PFL (not shown) passes through L_{dc} and then through the bypass L_v. Further two paths for I_g to load are directly to L_d and through the convolute C and large volume L. At point C the incoming generator current I_g splits into surface currents I, I_d, and I_g returning to the generator. Dotted and dashed contours are used for calculation of magnetic fluxes. The inset shows current splitting at the convolute C, where r shows one convolute post.

Figure 3 suggests such a modification on Zebra and corresponds to the scheme of Fig. 1(b) from Ref. [5]. The LCM consists of two concentric toroids connected to the load L_d through a post-hole convolute C. L_v is the vacuum inductance between the toroids.

We still consider that the load inductance L_d is constant and define it as that downstream of the convolute C, Fig. 3. We assume perfectly conducting electrodes and absence of current losses across the vacuum gaps everywhere in the system. The current I_g comes from the generator and it flows on the inner surface of the external electrode of the vacuum chamber which is the anode A. The current flowing on the surface of the opposite electrode has the same value and opposite direction. I_g finally returns to the generator on the surface of the central cathode K (see also Fig. 1). The same current I_g is on the surface of electrodes in the volumes L_{v1} and L_{v2}, as well as in L_{dc}. Current splitting occurs only at the convolute C where four vacuum lines (volumes L, L_{dc}, L_d, and L_{v2}) are connected together, see the inset of Fig. 3. We chose clockwise direction of the

currents I and I_d in the volumes L and L_d accordingly. Faraday's law for the external contour (dots) enclosing the generator and all the inductances shown in Fig. 3 implies

$$(L_0 + L_{\rm dc} + L_v)\frac{dI_g}{dt} + L\frac{dI}{dt} + L_d\frac{dI_d}{dt} + \rho I_g = V_{\rm oc}, \quad (4)$$

where I_g is the generator current in the inductances L_0, $L_{\rm dc}$, and $L_v = L_{v1} + L_{v2}$ [I_g is different from I_0 in Eq. (1) as the circuit is changed], I_d is the load current in the inductance L_d, Fig. 3, and I is the current inside large cavity L (magnetic flux extruder).

Then, use a contour including only the extruder inductance L and the load L_d (dashed contour in Fig. 3). We assume that the convolute inductance can be made small compared to that of the load. Choose counterclockwise path tracing of this contour so that the magnetic flux in L will contribute as $-LI$ (direction of the current I is opposite to the path-tracing direction), the flux in L_d will contribute as L_dI_d and the total flux will be equal to $-LI + L_dI_d$. This magnetic flux is zero inside this contour before the power pulse because the currents are zero. This flux is further conserved because we assume absence of dissipation in perfectly conducting electrodes, so it remains zero when the generator current starts. Therefore, we have for this contour at any time

$$LI - L_dI_d = 0. \quad (5)$$

Current splitting at the convolute C is illustrated by the inset of Fig. 3. Consider one convolute post r. The inflowing and outflowing currents for this post are shown by black arrows and they are $I + I_d$ and $I_g + I_g$ accordingly, so that the current continuity at the point C requires

$$I_d + I = 2I_g. \quad (6)$$

The same result can be obtained if we include more than one post or if we study inflowing and outflowing currents for the convolute holes (more precisely, for the spacing between holes) shown by gray arrows in the inset of Fig. 3.

Equations (4)–(6) thus describe the generator—LCM—load circuit changed with LCM modification of the vacuum region. From Eqs. (5) and (6) the currents inside the extruder and into the load are thus

$$I = \frac{2L_d}{(L + L_d)}I_g \qquad I_d = \frac{2L}{(L + L_d)}I_g. \quad (7)$$

Introducing the current multiplication coefficient $\kappa \equiv I_d/I_g$, one can see that for $L \gg L_d$ we have $I \ll I_g$ and $\kappa \to 2$, i.e. if the extruder cavity inductance is much higher than that of the load, the extruder current becomes much smaller than that of the generator while the generator current can be doubled. The generator current differs from I_0 in Eq. (1) and it is now described by (4) or by the following, substituting Eq. (7) into Eq. (4):

$$\begin{aligned} &L_{\rm tot}{}^*\frac{dI_g}{dt} + \rho I_g = V_{\rm oc} \\ &L_{\rm tot}{}^* \equiv L_0 + L_{\rm dc} + L_v + \frac{4LL_d}{L + L_d}. \end{aligned} \quad (8)$$

Simplifying our analysis we consider once more $V_{\rm oc}(t) = {\rm const}$, i.e., the "load-limited" regime defined above. As discussed, studying this regime allows a comparison of LCM performance even with an ideal PFL generator. The solution of Eq. (8) for the generator current will be the same as (2) except $L_{\rm tot}$ should be substituted by $L_{\rm tot}{}^*$. Equation (7) allows one then to find the modified load current I_d [cf. Eq. (2) defines the "old" current into load]:

$$I_d = \frac{2L}{(L + L_d)}\frac{V_{\rm oc}}{\rho}\left[1 - \exp\left(-\frac{\rho}{L_{\rm tot}{}^*}t\right)\right]. \quad (9)$$

Similarly to Eq. (2), we define the new current rise time as $t_d \equiv 2L_{\rm tot}{}^*/\rho$ and the new load current amplitude as $I_d{}^{\rm max} \equiv I_d(t_d)$, so that at $t = t_d$ the current I_d makes approximately 86% of its maximum possible value for $t \to \infty$. Defined in this way, the $I_d{}^{\rm max}$ value can reach 2 times the load current amplitude value $I_0{}^{\rm max}$ of the standard non-LCM configuration (Fig. 1) if $L \gg L_d$, so that advantage of the LCM is evident:

$$\begin{aligned} &I_g{}^{\rm max} \equiv I_g(t_d) = \frac{V_{\rm oc}}{\rho}(1 - e^{-2}) = I_0{}^{\rm max} \\ &I_d{}^{\rm max} \equiv I_d(t_d) = \frac{2L}{L + L_d}I_g{}^{\rm max} \to 2I_0{}^{\rm max} \\ &i_d{}^{\rm max} \equiv \frac{I_d{}^{\rm max}}{I_0{}^{\rm max}} = \frac{2L}{L + L_d} \to 2. \end{aligned} \quad (10)$$

However, as $L_{\rm tot}{}^* > L_{\rm tot}$, the characteristic current rise time t_d increases when the LCM is applied, i.e. $t_d > t_0$. In this case the load current maximum occurs later in time than in the no-LCM case and the I_d value at $t = t_0$ is obviously lower than $I_d{}^{\rm max}$. In order to investigate the efficiency of LCM operation in a more rigorous way, we normalize the load current of Eq. (9) to $I_0(t)$ from Eq. (2) and consider both $I_d(t)$ and $I_0(t)$ for $t = t_0$, $i_d \equiv I_d(t_0)/I_0(t_0)$. The case $i_d > 1$ would signify that the load current in Fig. 3 is higher even at the time where the no-LCM current is maximum. In turn, dimensionless value $\tau \equiv t_d/t_0$ would characterize the degree of current rise time increase when the modification of Fig. 3 is considered. Expressions for the normalized load current i_d and normalized current rise time τ are

$$i_d \equiv \frac{I_d(t_0)}{I_0(t_0)} = \frac{2L}{L + L_d}\frac{1 - e^{-2/\tau}}{1 - e^{-2}} \qquad \tau \equiv \frac{t_d}{t_0} = \frac{L_{\rm tot}{}^*}{L_{\rm tot}}. \quad (11)$$

For the sake of simplicity, suppose the value of $L_{\rm dc}$ to be the same both in Fig. 1 and in Fig. 3. Let us now neglect the bypass inductance value L_v, e.g. $L_v \ll L_0 + L_{\rm dc}$ in

Eq. (8). This condition is not automatically satisfied for all generators but it allows preliminary parametric study of a system with LCM. The normalized values of Eq. (11) can then be expressed as

$$i_d = \frac{2x}{d+x}\,\frac{1-e^{-2/\tau}}{1-e^{-2}} \qquad \tau = \frac{1+4xd/(x+d)}{1+d}, \quad (12)$$

where $x \equiv L/(L_0 + L_{dc})$ is the normalized extruder cavity inductance and $d \equiv L_d/(L_0 + L_{dc})$ is the normalized load inductance.

The values of i_d and τ from (12) are plotted in Fig. 4. This parametric analysis allows a preliminary estimate of the necessary LCM extruder volume L for given $L_0 + L_{dc}$ and L_d. The LCM load current I_d at $t = t_0$ can be made higher than the maximum current ${I_0}^{max}$ in standard generator configuration already at moderate extruder cavity inductance values. For example, for LCM with $x = 2$ and for $d = 0.25$, i.e., for $L_d = 0.25\,(L_0 + L_{dc})$, we have $I_d \approx 1.5\ {I_0}^{max}$ at $t = t_0$ ($i_d \approx 1.5$ in Fig. 4). In turn, ${i_d}^{max} = 2x/(x+d) \approx 1.78$ in Eq. (10) so that $I_d \approx 1.78 {I_0}^{max}$ at $t = t_d$ ($t_d \approx 1.5 t_0$ in Fig. 4). The region with $x < 1$ for $d = 0.25$ is not suitable even for an ideal PFL generator with $t_{0\,V} = 0$, Eq. (9), and an ideal LCM, $L_v = 0$, because application of an LCM would lead to the load current rise time increase, $\tau > 1$ with a moderate or no gain in the load current amplitude i_d. Similarly, the region with $x \gg 1$ should be more accurately studied from the viewpoint of a concrete engineering design because high L lead to higher bypass inductance L_v, see Fig. 3, which may become non-negligible.

If we allow t_d to be significantly greater than t_0, the LCM may potentially improve generator-to-load coupling and increase the load current above the no-LCM value even at higher load inductances than those presented in Fig. 4. For example, for $d = 1 (L_d = L_0 + L_{dc})$, for $x \gg 1$ ($L \gg L_0 + L_{dc}$), and when L_v can be still neglected ($L_v \ll L_0 + L_{dc}$), Eqs. (10) and (12) yield $i_d \approx 1.27$ and ${i_d}^{max} \to 2$ for $t_d \to 2.5 t_0$.

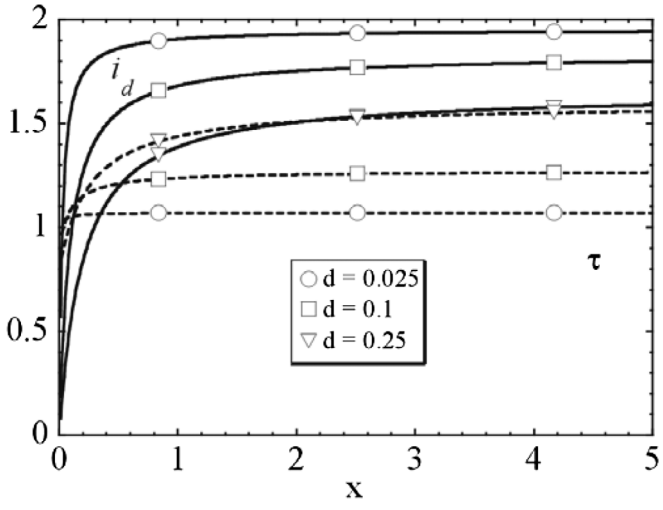

FIG. 4. Normalized load current i_d (solid lines) and rise time τ (dashed lines) as functions of normalized LCM extruder inductance x and for different normalized load inductances d, Eq. (12).

Therefore, the simplified analysis above suggests that the LCM technique proposed in Ref. [5] is capable to improve characteristics of a PFL generator operating on inductive loads without changing the generator parameters V_{oc}, ρ, and L_0. For an ideal PFL generator able to deliver electrical power during sufficient time, with $V_{oc} =$ constant, in the range of parameters discussed above the load current can be increased and have the same rise time t_0 as the no-LCM current. If the experiment allows $t_d > t_0$, the load current can be almost doubled.

Here we always considered inductive loads on PFL generators. Those loads correspond to a variety of solid-state and plasma loads in high-energy-density physics [1–13]. Figure 4 shows higher load current gains (higher i_d at given x) for smaller normalized load inductances d. In an LCM configuration the load inductance L_d is unambiguously defined as that downstream of the LCM convolute, Fig. 3. On the contrary, in a no-LCM case (standard pulse-power generator output, Fig. 1), the volume with constant inductance L_d cannot be distinguished from the rest of the vacuum volume and this is the reason why we could use only the experiment-dependent sum value $L_{dc} + L_d$, see Fig. 2.

In fact, LCM intentionally separates the small high-energy-density volume comprising physical processes under study from the rest of the vacuum volume in Fig. 2. In other words, the LCM technique implicitly assumes that (a) the load volume having constant inductance L_d (e.g. for obtaining high pulse magnetic fields [11]) or variable inductance ΔL_d (z pinches, see, e.g., Ref. [12]) is a small volume with high magnetic energy density (the minimum size of this volume can be limited from below by some additional requirements, such as peculiarities of the physical process in interest, diagnostics access, etc.), and that (b) the LCM convolute is positioned as close as possible to L_d (or ΔL_d) volume. This may allow one to have $d \ll 1$ in the notations of Eq. (12) and thus $i_d > 1$ in Fig. 4 or ${i_d}^{max} \to 2$ in Eq. (10).

Following this logic, we modify the vacuum section in Fig. 1 by adding additional hardware between the PFL output and the load as sketched in Fig. 3. The experimental hardware shown in Fig. 5 is designed to operate in vacuum and it comprises magnetically insulated transmission lines (MITL) L_{v1} and L_{v2}, a large-volume magnetic flux extruder L and a post-hole convolute C (eight posts at the diameter of 18 cm). The procedure of electrical description of this system presented above concludes that the generator current tends to pass 2 times through the load in an ideal case, when $L \gg L_d$, because in this case we have $I \to 0$ in Eq. (6) and thus $I_d \to 2I_g$ in Eqs. (6) and (7).

In the experimental configuration of Fig. 5 the inductances in Eqs. (7) and (8) are: $L_0 \approx 26$ nH (unchangeable),

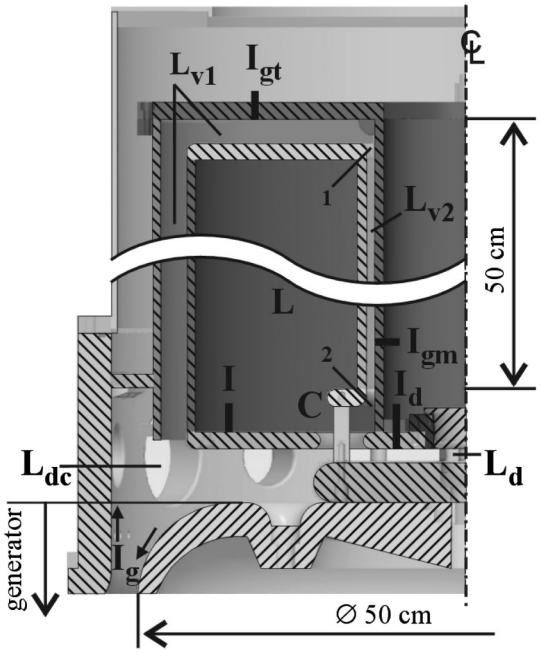

FIG. 5. Cylindrical geometry of the final LCM design for the Zebra generator. The interelectrode gaps in L_{v1} and L_{v2} parts are 2 cm and 6 mm accordingly, $L_v = L_{v1} + L_{v2}$. Shown are the locations of current measurements, each location corresponds to three azimuthally distributed differential Bdots. The generator current I_g is measured by Bdots at the LCM top, I_{gt}, and near the convolute C, I_{gm}. The current inside the large flux extruder cavity is measured by the Bdots I. The load current is measured by the Bdots I_d. Distribution of current in the LCM is the same as in Fig. 3. L_d is the load represented either a 6-mm-diameter rod or a 12-mm-width (~ 1 mm thickness) strip installed at the axis of the system, both in stainless steel and 1 cm height. The inductance L_d is calculated as that between the axial electrode and the LCM convolute posts (eight posts, each having diameter of 12 mm).

$L_{\rm dc} \approx 9$ nH (diagnostic chamber), $L \approx 90$ nH (large LCM cavity), $L_v = L_{v1} + L_{v2} \approx 24$ nH (LCM MITL's). Therefore, the region around $x \sim 2.5$ was chosen from the idealized analysis of Fig. 4. The L_v value was then obtained from choosing some realistic interelectrode gap sizes in the bypass region. The load was either a 6-mm-diameter rod or a 12-mm-width (~ 1 mm thickness) strip, both installed at the axis of the system. The inductance between the axial electrode and eight posts of the LCM convolute was $L_d \approx 7$ nH. Under assumption of no current losses in the vacuum gaps, the theoretical load current multiplication coefficient $\kappa = I_d/I_g$ from Eq. (7) is $\kappa \approx 1.86$.

Figure 6 illustrates the experimental currents recorded on Zebra after the modification of Fig. 5 were made. Locations of the current measurements is are shown in Fig. 5 (three azimuthally distributed differential Bdots at each level for I_{gt}, I_{gm}, I, and I_d). Each curve of Fig. 6 is found as an average of Bdot signals for each level.

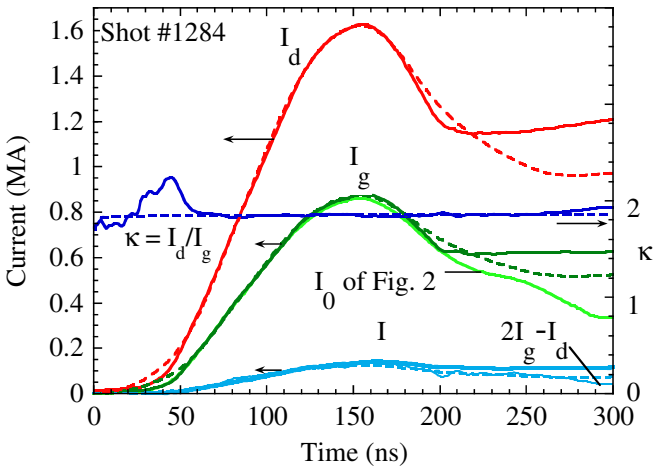

FIG. 6. (Color) Experimental currents (solid lines) measured in the configuration of Fig. 5. I_d, I_g, and I are the load, generator, and extruder currents accordingly. The load was a 6-mm-diameter on-axis rod. Dashed lines are the numerical solution of Eqs. (7) and (8) with the $V_{\rm oc}(t)$ from Fig. 2 increased by 6% to match this experiment. Also shown for comparison is the measured load current I_0 in nominal Zebra operation, Fig. 2.

There was no difference between two generator current measurements, $I_{gm} \approx I_{gt} = I_g$, which signifies no current losses in the 6-mm-gap L_{v2} MITL. The estimated electric field in this vacuum line could reach 370 kV/cm at the top (point 1 in Fig. 5) and 250 kV/cm at the bottom (point 2 in Fig. 5) in the discussed shot. The losses were also absent in other parts of the system as the experimental current multiplication $\kappa \equiv I_d/I_g$ was almost identical to the theoretical value (that assumed no losses) during a great portion of the current pulse, Fig. 6 (early spike on κ waveform is due to the measurement uncertainty/asymmetry when the currents are still small). Numerical solutions of the system (7) and (8) for I_g, I_d, and I are plotted as dashed lines and they coincide with corresponding experimentally recorded waveforms during the time when $V_{\rm oc}(t)$ data can be trusted, see Fig. 2. Also, the analytical extruder current $I = 2I_g - I_d$ (I_g and I_d are experimental), Eq. (6), coincide with the measured $I(t)$. All above-mentioned validates the analytical description of LCM we used.

Table I summarizes results of the experiments performed in the discussed setup. Experimental peak generator currents I_g, peak load currents I_d, and load current rise times $t_d^{\rm exp}$ defined in the same way as in Fig. 2 and current multiplication coefficients κ at peak current are listed. The measured κ is always close to the theoretical value within error bars indicating lossless operation of the setup of Fig. 5 on Zebra.

In the shot of Fig. 6, the load current reached 1.62 MA with practically unchanged current rise time $t_d^{\rm exp} = t_{\rm peak} - t_{\rm start} = 116$ ns if compared to $t_d^{\rm exp}$ in the nominal shot of Fig. 2. Indeed, the values of L_d, L, L_v, and $L_{\rm dc}$ realized in practice result in $L_{\rm tot}^* \approx 85$ nH, Eq. (8), and in

TABLE I. Peak experimental currents and κ values for configuration of Fig. 5 (relative scattering of peak value due to uncertainty/asymmetry in parentheses). $L_d \approx 7$ nH and theoretical $\kappa \approx 1.86$ in all shots with LCM. Shot #1284 with LCM is shown in Fig. 6. Shot #1286 with LCM had a strip load with 12 mm width instead of 6-mm-diameter rod. Shot #1275 (Fig. 2) for Bdots calibration in standard Zebra configuration (Fig. 1) is included for comparison. $L_{\mathrm{tot}}^{(*)}$ denotes L_{tot} from Eq. (3) in standard configuration and L_{tot}^{*} from Eq. (8) in LCM configuration.

Shot #	1284	1285	1286	1275
Configuration	LCM	LCM	LCM	Standard
Load	rod ⌀6 mm	rod ⌀6 mm	strip 12 mm	rod ⌀6 mm
$L_{\mathrm{tot}}^{(*)}$ (nH)	85	85	85	66
I_g (MA)	0.88(±24%)	0.83(±9%)	0.78(±12%)	0.86
I_d (MA)	1.62(±8%)	1.54(±11%)	1.59(±6%)	0.86
t_d^{exp} (ns)	116	113	115	114
κ	1.84(±25%)	1.85(±14%)	2.04(±13%)	1

theoretical $t_d \approx 89$ ns $< t_{0\,\mathrm{V}} \sim 100$ ns. Therefore, the chosen LCM configuration still allows the "generator-limited" regime on this concrete generator and therefore does not lead to t_d^{exp} increase.

The magnetic field on the load rod surface reached the megagauss level in the experiment of Fig. 6 with the estimated value of 1.08 MG. The load magnetic energy in the volume associated with $L_d = 7$ nH was increased from 2.6 to 9.2 kJ which corresponds to an improved driver-to-load energy transfer efficiency. Figure 7 shows that, for obtaining the same performance in the standard configuration of Fig. 1, the generator voltage amplitude V_{oc} would have to be increased almost twice. This would lead to the stack voltage increase 2.8 times if compared to the nominal Zebra configuration, Fig. 2, and 1.8 times if compared to the LCM operation, Fig. 6, possibly requiring an increase in L_0.

Such an increase of the generator voltage would require major changes of generator energetics and architecture. Instead, the observed enhanced load currents and load magnetic energies are obtained using the LCM technique at low cost and without modifying the generator. This capability will allow high-energy-density physics research at higher levels of magnetic field on Zebra. In particular, envisaged applications with constant-inductance loads on Zebra are the studies of plasma–magnetic field interaction and experimental modeling of space plasmas in the laboratory [11]. Applications of the LCM technique to the loads having variable inductance $L_d(t) \neq$ const or/and non-negligible resistance, such as planar wire-array z pinches [12] are already in progress on this generator [13].

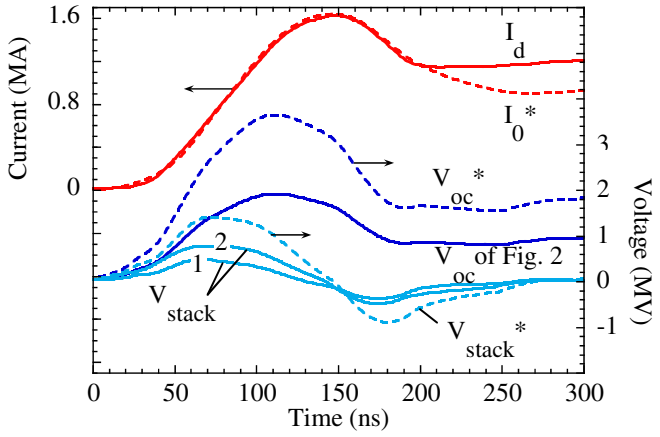

FIG. 7. (Color) Experimental currents and voltages (solid lines): nominal generator open-circuit voltage V_{oc}, (1)—nominal voltage on the insulator stack V_{stack} in no-LCM configuration, (2)—stack voltage in the LCM shot of Fig. 6 and the load current I_d in this shot. Numerical solution of Eq. (1) (dashed lines): the same load current amplitude of 1.6 MA could be reached only if the generator energetics is increased, i.e., if the generator voltage is 1.9 times higher, $V_{\mathrm{oc}}^{*} = 1.9 V_{\mathrm{oc}}$. (3)—The peak stack voltage V_{stack} would rise from nominal 0.5 to 1.4 MV in this case.

ACKNOWLEDGMENTS

We thank Dr. J. L. Porter for support of this work. We would like to thank the referee for helpful discussions. This work is supported by Sandia National Laboratories under DOE/SNL Contracts No. 681371, No. 686929, and No. 530307, by CNRS, France, by DOE/DGA-SNL/CEG agreement, by DOE under NNSA Cooperative Agreements No. DE-FC52-06NA27586, No. DE-FC52-06NA27588, and in part by No. DE-FC52-06NA27616. Sandia is a multiprogram laboratory operated by Sandia Corporation, a Lockheed Martin Company, for the United States Department of Energy's National Nuclear Security Administration under Contract No. DE-AC04-94AL85000.

[1] V. M. Titov and G. A. Shvetsov, *Megagauss Fields and Pulsed Power Systems* (Nova Science Publishers, New York, 1990).
[2] M. K. Matzen *et al.*, Phys. Plasmas **12**, 055503 (2005).
[3] J. P. VanDevender, in *Proceedings of the 3rd International Pulsed Power Conference*, edited by T. H. Martin and A. H. Guenther (IEEE, New York, 1981), pp. 248–251.

[4] W. A. Stygar, M. E. Cuneo, D. I. Headley, H. C. Ives, R. J. Leeper, M. G. Mazarakis, C. L. Olson, J. L. Porter, T. C. Wagoner, and J. R. Woodworth, Phys. Rev. ST Accel. Beams **10**, 030401 (2007).

[5] A. S. Chuvatin, L. I. Rudakov, B. V. Weber, R. Cadièrgues, and F. Bayol, Rev. Sci. Instrum. **76**, 063501 (2005).

[6] A. S. Chuvatin, A. A. Kim, V. A. Kokshenev, B. M. Kovalchuk, A. V. Shishlov, A. V. Fedunin, A. Yu. Labetsky, N. A. Zhidkova, N. E. Kurmaev, F. I. Fursov, F. Lassalle, H. Calamy, and M. Krishnan, in Proceedings of the 16th IEEE International Pulsed Power Conference, 2007, Albuquerque, New Mexico (unpublished).

[7] J. S. Shlachter, Plasma Phys. Controlled Fusion **32**, 1073 (1990).

[8] B. S. Bauer, V. L. Kantsyrev, N. Le Galloudec, R. Presura, G. S. Sarkisov, A. S. Shlyaptseva, S. Batie, W. Brinsmead, H. Faretto, B. LeGalloudec, A. Oxner, M. Al-Shorman, D. A. Fedin, S. Hansen, I. Paraschiv, H. Zheng, D. McCrorey, J. W. Farley, J. Glassman, and J. S. De Grootin, in *Proceedings of the 12th International Pulsed Power Conference*, edited by Charles Stallings and H. Kirbie (IEEE, New York, 1999), pp. 1045–1047.

[9] http://www.ntf.unr.edu/zebra.php.

[10] R. B. Miller, *An Introduction to the Physics of Intense Charged Particle Beams* (Plenum Press, New York, 1982).

[11] W. Horton, C. Chiu, T. Ditmire, P. Valanju, R. Presura, V. V. Ivanov, Y. Sentoku, V. I. Sotnikov, A. Esaulov, N. Le Galloudec, T. E. Cowan, and I. Doxas, Adv. Space Res. **39**, 358 (2007).

[12] V. L. Kantsyrev, L. I. Rudakov, A. S. Safronova, A. A. Esaulov, A. S. Chuvatin, C. A. Coverdale, C. Deeney, K. M. Williamson, M. F. Yilmaz, I. Shrestha, N. D. Ouart, and G. C. Osborne, Phys. Plasmas **15**, 030704 (2008).

[13] A. S. Chuvatin, V. L. Kantsyrev, L. I. Rudakov, M. E. Cuneo, A. L. Astanovitskiy, R. Presura, A. S. Safronova, A. A. Esaulov, W. Cline, K. M. Williamson, I. Shrestha, M. F. Yilmaz, G. C. Osborne, M. Weller, T. Jarrett, B. LeGalloudec, V. Nalajala, T. D. Pointon, and K. A. Mikkelson, AIP Conf. Proc. **1088**, 253 (2009).